Modeling the dynamics of a free boundary on turbulent thermal convection

Jin-Qiang Zhong[1] and Jun Zhang[1,2]
[1]*Center for Soft Matter Research, Department of Physics, New York University, 4 Washington Place, New York, New York 10003, USA*
[2]*Applied Mathematics Laboratory, Courant Institute of Mathematical Sciences, New York University, 251 Mercer Street, New York, New York 10012, USA*

(Received 13 November 2006; published 16 July 2007)

Based on our previous experimental study, we present a one-dimensional phenomenological model of a thermal blanket floating on the upper surface of a thermally convecting fluid. The model captures the most important interactions between the floating solid and the fluid underneath. By the thermal blanketing effect, the presence of the solid plate modifies the flow structure below; in turn, the flow exerts a viscous drag that causes the floating boundary to move. An oscillatory state and a trapped state are found in this model, which is in excellent agreement with experimental observations. The model also offers details on the transition between the states, and gives useful insights on this coupled system without the need for full-scale simulations.

DOI: 10.1103/PhysRevE.76.016307 PACS number(s): 47.20.Bp, 47.27.te

I. INTRODUCTION

A large number of works have been devoted to the investigation of turbulent Rayleigh-Bénard convection [1–4], a phenomenon that occurs when a fluid is heated from below and cooled from above and is enclosed within rigid boundaries. One of the central issues of these studies is to determine the overall efficiency of heat transport through the fluid, which depends on the temperature difference between the top and the bottom, the thermal properties of the chosen fluid, the shape of the container [5–7], and also the mechanical and thermal properties of the boundaries [8–11].

In turbulent thermal convection, coherent structures emerge despite the turbulent features of the flows. One of these structures is a large-scale circulation (LSC) that is driven by and, in turn, entrains the thermal plumes that detach from the two horizontal boundary layers [12]. This flow structure has attracted wide attention since it is able to change the statistical properties of the thermal fluctuations of the driven system [13]. Recent elaborate experiments studied the rotation and cessation dynamical states of these large-scale flows in a rigid cylindrical enclosure [14,15].

As a ubiquitous phenomenon in nature, thermal convection often interacts with movable structures. It is of fundamental interest to study the dynamic behavior of a convective fluid that is coupled to a mobile boundary. In particular, we study a convective fluid with a freely-moving boundary on top of the fluid surface. We seek to find out if the flow structure and its temporal behavior remain qualitatively the same as that with rigid boundaries and if the interaction between the mobile boundary and the convective fluid leads to new dynamical states.

One similar problem that concerns a freely moving boundary coupled with turbulent thermal convection is the geophysical phenomenon of mantle convection interacting with overlying continents [16]. A mechanism involving a large insulating plate drifting upon cellular convective flows has been suggested as a laboratory model in studying continental drift [17]. This phenomenon was also modeled experimentally as a freely moving heat source that floats on top of a fluid [18,19]. Recent numerical simulations of such interactions have revealed rich dynamics including interesting periodic states of continental motion and intermittent continental collisions and breakups [20–23].

Our previous experiments studied the interaction between a single floating boundary and a turbulent convecting fluid [24–26]. Despite the turbulent nature of the flows, we found that the motion of the floating boundary is relatively simple and can be well classified into two states: an oscillatory state with small floating boundaries, and a trapped state with larger floating boundaries.

We attempt to model the essential physical mechanism that leads to the emergence of these two states. Indeed, direct full-scale simulation of turbulent thermal convection with a freely moving boundary is quite challenging. For one, the dynamics of high Rayleigh number convection depends heavily on the fine details at the thin boundary layers, regions with most thermal activity. For another, the problem involves thermal and mechanical coupling of the turbulent fluid with a time-dependant boundary condition [20–23].

Instead, based on our experimental observations (Sec. II), we develop a phenomenological model to describe the one-dimensional motion of the freely moving top boundary. The model starts with a description of the convection system (Sec. III), where we include the crucial elements of the boundary-fluid interaction. The viscous drag applied by the underlying large-scale circulations drives the floating boundary. In turn, the floating boundary acts like a thermal blanket for the fluid, and rearranges the flow pattern in the convective bulk due to heat flux redistribution.

We then present in Sec. IV the results of the model, which includes the motion of the floating boundary and the corresponding evolution of the flow pattern. A dynamical transition is identified: the free-boundary motion changes from an oscillatory state to a trapped state as the boundary size exceeds a critical size. This result is compared with our experimental data. Our simple model predicts both the oscillation periods in oscillatory state and the convergent rates in the trapped state. They depend sensitively on the floating boundary size.

The stability of the model is further analyzed in Sec. V. The equation of motion is analyzed as a linear delayed-differential equation (DDE), which is then solved in closed

form. There, stable solutions correspond to the trapped state and unstable solutions correspond to the oscillatory state. The critical condition for the dynamical transition is obtained analytically.

In the appendixes, we discuss several constants used in the model that we determine from our previous experimental results. How the critical boundary size depends on these constants is shown in phase diagrams.

II. THE EXPERIMENTAL OBSERVATIONS

In our recent experiments [25,26], a rigid, freely-moving boundary floats on the surface of a Bénard convection cell. There is thus a heterogeneous thermal boundary condition at the top surface of the fluid. The convection cell is a rectangular, lidless tank with sizes of 36.5 cm (length: D), 7.8 cm (width: W), and 11.3 cm (height: H). The width (w) of the floating boundary covers most (88%) of the width (W) of the convection cell (Fig. 1). Its length d is changed incrementally from 7.2 to 29.2 cm. Thus the coverage ratio d/D varies between 0.2 and 0.8. The motion of the floating boundary is confined within one dimension, along the long axis of the convection cell, and is determined by the viscous force from the convective flows underneath. The fluid inside is heated uniformly at the bottom and cooled at the surface. In the experiment, the applied vertical temperature difference ΔT across the convection cell is kept constant; the Rayleigh number for the system is thus

$$\mathrm{Ra} = \frac{\alpha g \Delta T H^3}{\nu \kappa} = 1.1 \times 10^9.$$

Here g is the gravitational acceleration and α, ν, and κ the thermal expansion coefficient, the kinematic viscosity, and the thermal diffusivity of the fluid, respectively.

In the presence of a floating boundary on the free fluid surface, we observe in the experiment that two large-scale circulations coexist and occupy the entire volume of the cell. As shown in Fig. 1, these two large-scale circulations counter-rotate, sharing in between a common upwelling flow. The mechanism that creates this upwelling structure is similar to the thermal blanketing effect in geophysics [23,25,27,28]. As the top-boundary partially covers the open fluid surface, convective flows underneath are prohibited from reaching the fluid surface, thus the local vertical heat flux is greatly reduced. Away from the floating boundary, the convecting fluid experiences effective cooling. As a result, heat builds up within the fluid that lies below the solid boundary. An upwelling under the floating boundary is thus induced. Due to the net force it experiences from the flows, the floating boundary changes position. The aforementioned heat blocking effect continues to take place and the floating boundary apparently "attracts" the upwelling. Indeed, the upwelling migrates toward the bottom of the floating boundary at a longer time-scale than the transit time of the floating boundary. During this longer time-scale, the flow structure reorganizes itself to adapt the changed top boundary condition.

Figures 1(a)–1(e) show five snapshots that demonstrate this thermal blanketing effect. An upwelling was initially induced by the floating boundary near the left side of the convection cell and the boundary is then driven by the clockwise large-scale circulation to the right end of the cell [Fig. 1(a)]. For a short period of time, the system is stable: the clockwise circulation pushes the floating boundary against the right side of the cell wall. However, this coupled system is not stable over a long time. Thermal blanketing causes the upwelling to migrate toward the bottom of the floating boundary, as shown in Figs. 1(a)–1(d). We observe that the upwelling drifts toward the center of the floating boundary at a gradually decaying rate. During this process, the counterclockwise eddy on the left side expands at the expense of the clockwise eddy on the right. Just before the upwelling has converged to a position below the center of the floating boundary, the stronger counterclockwise eddy drags the boundary away to the left side of the tank [Fig. 1(e)].

Also due to the thermal blanketing effect, we observe that the speeds of the two large-scale circulations change in re-

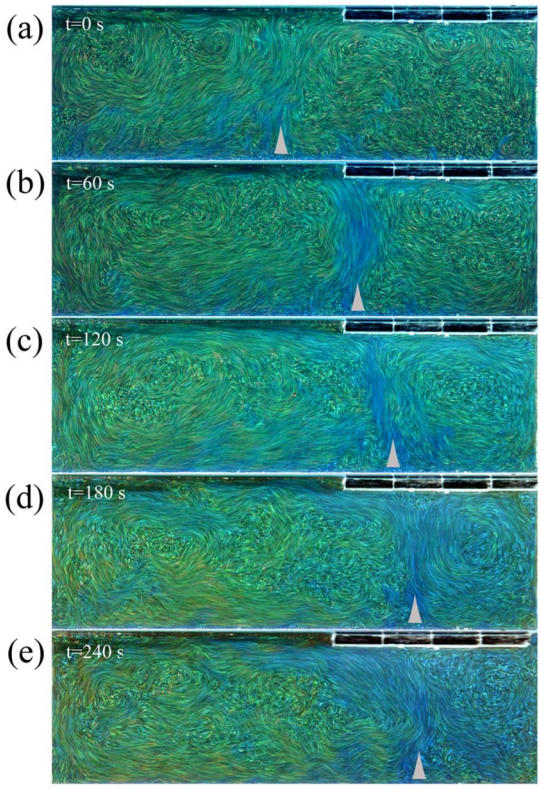

FIG. 1. (Color online) Flow visualization from the experiment showing the migration of the upwelling due to thermal blanketing. The experiment runs at $\mathrm{Ra}=1.1\times10^9$, and the floating boundary covers 40% of the upper fluid surface ($d/D=0.4$). The turbulent flows are visualized using thermochromic liquid-crystal beads that are evenly suspended in the fluid bulk. Each photo uses an exposure time of 1.3 s. The colors of the beads change gradually from blue to yellow as the local temperature decreases. Small gray triangles indicate the horizontal positions of the upwelling. (a) At $t=0$ s, the floating boundary is at the right side and the upwelling is located near the cell center. Photos (b), (c), and (d) show the upwelling drifting rightward, slowing down as it approaches the center of the floating boundary. (e) As the net force acting on the floating boundary switches direction, from right to left, the boundary starts to move to the left.

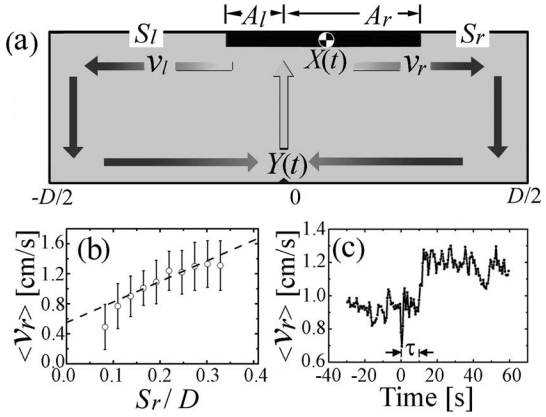

FIG. 2. (a) An illustration for the fluid-loop model used in our analysis (see text for detail). (b) The mean flow speed of the circulation on the right v_r increases monotonically as the linear span of the open fluid surface (S_r, on the right) widens. The dashed line indicates the slope and the offset used in our model [$v_0 = 0.55$ cm/s and $\theta = 0.075$ s^{-1}, see Eq. (6)]. (c) The flow response has a short delay, $\tau = 10$ s. At $t = 0$, we relocate the floating boundary so that S_r changes from 5 to 10 cm. After the delay, v_r adapts to a new value. The data shown here is an average over 30 identical measurements. Figure adapted from Zhong and Zhang [26].

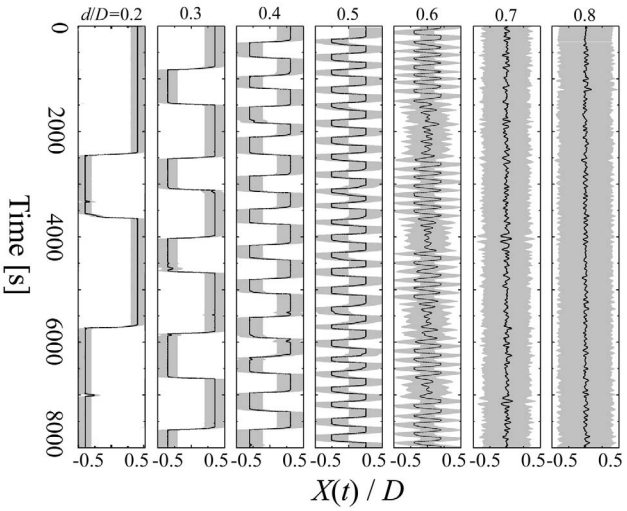

FIG. 3. Experimental data for the motion of floating boundary at different sizes. The position of the floating boundary is normalized by the cell length D. From left to right, the coverage ratio is increased incrementally from 0.2 to 0.8. The solid lines show the center of mass of the boundary and the gray areas indicate the spatial extent of the floating boundary. Figure adapted from Zhong and Zhang [26].

sponse to the movement of the floating boundary (Fig. 2). Increased fluid surface exposure leads to a greater number of downwelling cold plumes and to a faster large-scale circulation. As shown in Fig. 2(b), the circulation speed within either one of the eddies increases monotonically as the corresponding linear extension of the open fluid surface increases.

The floating boundary constantly modifies the underlying flow pattern and changes the circulation strength. In turn, the viscous force generated by the convective flows determines the motion of the floating boundary. These two feedback mechanisms lead to two interesting dynamical states. Figure 3 shows typical experimental results, which was discovered previously [26]. For a small floating boundary, $d/D = 0.2$, the oscillation period is long and less regular. The oscillation becomes more regular with shorter periods as the size of the floating boundary increases. As the size of the floating boundary is further increased ($d > 0.6D$), a different dynamical state appears: the floating boundary is localized near the center of the convection cell, with small-amplitude, random excursions to both sides. We refer to this state as the trapped state. The transition happens around a critical size with $d/D = 0.6$, where large-amplitude oscillations and localized motions appear alternatively.

III. THE ONE-DIMENSIONAL PHENOMENOLOGICAL MODEL

Based on our experimental observation, we now develop a one-dimensional, phenomenological model that describes the motion of a solid boundary floating above two counterrotating convective circulations [Fig. 2(a)]. We present here the rich behaviors of the modeled system and a detailed account of the related analyses, which were previously lacking in our earlier paper [26] when the model was first introduced.

In this model, we consider the following two factors: (1) due to thermal blanketing, the floating boundary attracts the upwelling from anywhere in the convection cell to a position right below the center of the boundary and (2) the net viscous force exerted by the convective flow determines the instantaneous motion of the floating boundary. A viscous boundary layer exists next to the rigid floating boundary. The net viscous force applied at the base of the boundary is

$$T(t) = w \int_{x_1}^{x_2} \sigma_{xz}(x,t) dx \tag{1}$$

Here x_1 and x_2 are the coordinates of the left and right edges of the floating boundary. For an incompressible fluid, the stress tensor near a horizontal rigid boundary is $\sigma_{xz}(x,t) = \eta \frac{\partial u_x(x,t)}{\partial z}$, where $u_x(x,t)$ is the horizontal component of the flow speed near the floating boundary, and η is the dynamic viscosity.

The geometric center of the floating boundary is denoted by $X(t)$. As a rigid body, the velocity everywhere on this boundary is $\dot{X}(t)$. The fluid velocity gradient next to the boundary is approximated

$$\frac{\partial u_x(x,t)}{\partial z} \approx \frac{v_{\text{flow}}(x,t) - \dot{X}(t)}{\lambda}, \tag{2}$$

where λ is the thickness of the viscous boundary layer next to the floating boundary and $v_{\text{flow}}(x,t)$ is the horizontal component of the flow speed just outside the viscous boundary layer.

Now we consider the dynamical equation of motion. The viscous shear force T applied at the floating boundary bottom in Eq. (1) is the driving force for the boundary motion. Most

of the floating boundary is immersed within the fluid (Fig. 1); all its four lateral edges experience a viscous resistance, which opposes its motion. Assuming that the motion of the boundary is overdamped in the surrounding fluid at Reynolds number ~50, the resistance and the viscous driving force are balanced with each other. Thus we neglect the inertia of the floating boundary. The equation of motion is thus

$$T(t) = \gamma \eta \dot{X}(t). \tag{3}$$

Here γ is a geometry factor depending on the dimensions of the floating boundary [29].

Combined with Eqs. (1) and (2) the equation of motion (3) becomes

$$\dot{X}(t) = \frac{1}{\gamma \lambda / w + d} \int_{x_1}^{x_2} v_{\text{flow}}(x,t) dx. \tag{4}$$

Equation (4) shows that the motion of the rigid floating boundary of a given shape is uniquely determined by the flow velocity field near its base.

Experiments and numerical simulations show that a floating boundary on a thermally convecting fluid attracts the underlying upwelling; the migrating speed of the upwelling depends on both the size of the boundary and the distance from the upwelling to the boundary center [25,30,31]. Indeed, a rigorous description of the dynamical evolution of the flow pattern requires an exhaustive study on thermal convection and its interplay with a floating boundary. Instead, however, in our current model, we make various simple yet physical assumptions.

We assign the horizontal position of the upwelling as $Y(t)$. Function $G(x,Y)$ denotes the contribution from a unit segment length on the floating boundary at position x, to the migration speed of the upwelling. As shown in Fig. 1, the migration speed of the upwelling slows down as it approaches the boundary center. We therefore assume that the function $G(x,Y)$ is proportional to the distance between a unit segment and the upwelling $(x-Y)$. We thus have the function form $G(x,Y)=\beta(x-Y)$. Factor β is the proportionality constant. Since every part of the floating boundary contributes to the migrating speed of the upwelling, given that $x_2+x_1=2X$ and $x_2-x_1=d$, the migrating speed of the upwelling becomes

$$\dot{Y}(t) = \int_{x_1}^{x_2} G(x,Y) dx = d\beta [X(t) - Y(t)]. \tag{5}$$

In turbulent thermal convection, cold and hot thermal plumes randomly detach from the top and bottom thermal boundary layers, causing the local flow speed to fluctuate [32,33]. Since the size and mass of the floating boundary is much larger than that of the thermal plumes, local velocity fluctuations are averaged out and the motion of the boundary becomes smooth [25]. We thus can overlook the stochastic spatial structure of the flow velocity $v_{\text{flow}}(x,t)$ and instead use $v_i(t)$ $(i=l,r)$ as the mean flow speed for the circulations, where i indicates left or right. The flow speed $v_i(t)$ is spatially constant over the circumference of each convective circulation, as illustrated in Fig. 2(a). This approximation is analogous to the "fluid loop model," which was used as a scheme to model fluid circulation with heterogeneous boundary conditions, and has been applied to studies of turbulent thermal convection [34–37].

The mean flow speed $v_i(t)$ is time dependent since it responds to the changing position of the top boundary. As shown in Fig. 2(b) and 2(c), the position of the floating boundary influences the flow strength of the two convective circulations. Different exposed fluid areas give rise to different circulation speeds for the large circulating eddies. The response of the flow speed takes place with a short delay, τ. Given these considerations, the flow velocity of each convective circulation $v_i(t)$ is taken to depend linearly on the linear span of the above open surfaces at a previous moment

$$v_i(t) = v_0 + \theta S_i(t-\tau). \tag{6}$$

The offset v_0 and slope θ are determined from experimental data (see Appendix A).

Due to the contributions from the two counter rotating circulations, the right-handside of Eq. (4) is divided into two parts: an integral for the counterclockwise circulation (on the left) and one for the clockwise circulation (on the right)

$$\int_{x_1}^{x_2} v_{\text{flow}}(x,t) dx = \int_{x_1}^{x_2} v_i(t) dx = -v_l(t) A_l(t) + v_r(t) A_r(t).$$

A_i $(i=l,r)$ is the partial area of the floating boundary that lies on top of each circulation [38]. Combining Eqs. (4)–(6) we obtain

$$\dot{X}(t) = \frac{1}{d + \gamma \lambda / w} \{[2v_0 + \theta(D-d)][X(t) - Y(t)] - \theta d X(t-\tau)\},$$
$$\dot{Y}(t) = \beta d [X(t) - Y(t)]. \tag{7}$$

Additionally there are spatial constrains that both the floating boundary and the upwelling must lie between the two rigid side walls, namely,

$$-\frac{D-d}{2} \leqslant X(t) \leqslant \frac{D-d}{2}, \quad -\frac{D}{2} \leqslant Y(t) \leqslant \frac{D}{2}. \tag{8}$$

The boundary condition (8) is treated as follows. As the floating boundary arrives at the side boundary $[|X|=(D-d)/2]$, it is set to be at rest at the sidewall, $\dot{X}(t)=0$. Meanwhile the underlying flow structure evolves and the horizontal position of the upwelling $Y(t)$ approaches towards the center of the boundary. The floating boundary remains immobile until the net force from the flows switches direction and starts to drive the floating boundary away from the sidewall. Equation (7) with boundary conditions (8) form a closed system. In the model, the only parameter we vary is the size of the floating boundary d. Appendix A is a discussion on how we determine the constants $(\gamma\lambda/w, v_0, \theta, \beta, \tau)$.

IV. NUMERICAL RESULTS FROM THE MODEL

The results of the simple model are shown in this section. We leave the discussion on the relevant methods to Appendix

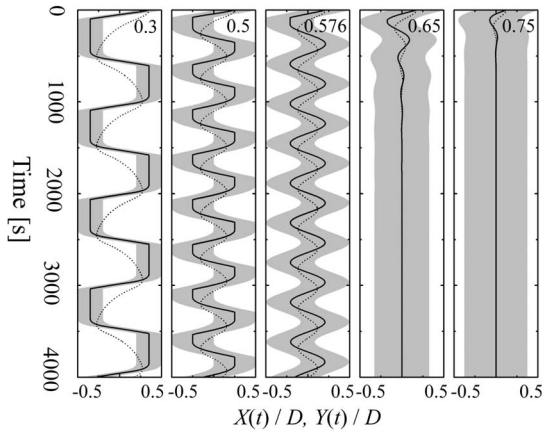

FIG. 4. Numerical simulation of the motion of the floating boundary. From left to right, the coverage ratios are 0.3 0.5, 0.576, 0.65, and 0.75. Time series of the floating boundary (solid lines) and the upwelling (dashed lines) are shown. Gray areas indicate the spatial extent of the boundary. Figure adapted from Zhong and Zhang [26].

A. Figure 4 shows the solutions of the dynamical equation (7) for different sizes of the floating boundary.

The coupled system experiences a transition from an oscillatory state to a trapped state as the floating boundary size exceeds a critical size. The first two panels in Fig. 4 illustrate the periodic oscillations of both the floating boundary and the upwelling, with $d/D=0.3$ and 0.5. Within each period, the floating boundary transits twice across the center of the cell. Between each transition there is a long waiting period as the floating boundary stays at one of the two sides. The floating boundary velocity goes to zero as soon as it collides with the sides. The upwelling follows behind the moving boundary. Its drifting velocity decreases as it approaches the floating boundary.

Figure 5 shows in close-up the relative positions of the floating boundary and the upwelling in an oscillatory state when $d/D=0.3$. Figure 5(a) shows an instant when the boundary stays on the left while the upwelling drifts towards the center of the boundary. During this time, the clockwise

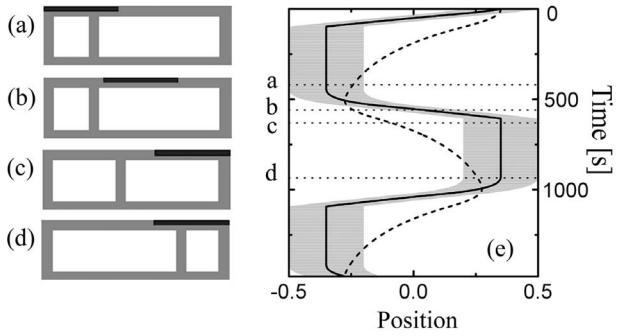

FIG. 5. (a)–(d) Four instances show the positions of the floating boundary and the upwelling over about half a period in an oscillatory state when $d/D=0.3$. The corresponding moments are indicated by four horizontal dotted lines in the time series (e). Solid line shows the position of the floating boundary and the dashed line shows the position of the upwelling flow.

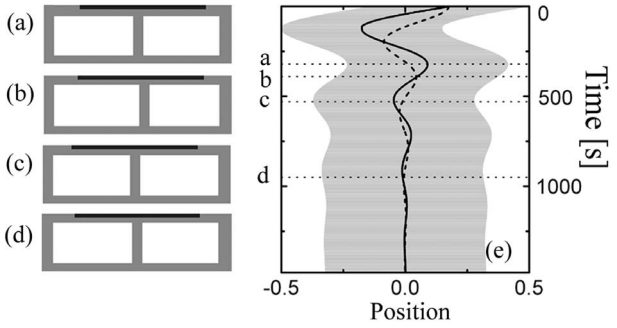

FIG. 6. In a trapped state, $d/D=0.65$, four snapshots (a)–(d) show the decaying oscillations of the floating boundary and the upwelling. The corresponding moments are indicated by four horizontal dotted lines in the time series (e). Solid line shows the position of the floating boundary and the dashed line shows position of the upwelling flow.

circulation on the right expands and gains speed as the counterclockwise circulation on the left shrinks and loses strength. Before the upwelling arrives under the center the floating boundary, the latter starts to move to the right since the net viscous drag switches from leftward to rightward. The upwelling changes direction and follows the boundary to the right [Fig. 5(c)]. This process continues and an oscillatory state emerges.

The dynamics of the coupled system with a sufficiently large floating boundary are different. The last two panels in Fig. 4 ($d/D=0.65$ and 0.75) show that both the floating boundary and the upwelling converge from their initial position to the center of the convection cell. They undergo a few decaying oscillations. Figure 6 illustrates this convergent process. Figure 6(a) shows an instant when the floating boundary changes direction at the right extreme of its trajectory during its motion. Following behind the boundary, the upwelling is still on the left side of the floating boundary. The partial area of the floating boundary lies on top of the right circulation A_r is greater than that on the left A_l. The floating boundary would seem to continue its rightward motion. However, at this moment the open fluid surface on the left S_l is greater than S_r, which strengthens the left circulation. Such response takes a delay time much shorter than the transition time of the boundary [Fig. 2(c)]. As a result, we find in the model that the difference in strength of the two circulations subsumes the difference in the areas of the floating boundary that are subject to viscous forces in different directions. Experiencing a stronger driving force leftward, the floating boundary moves back to the left and overshoots the center by a smaller amplitude [Figs. 6(b) and 6(c)]. After a few decaying oscillations, both the floating boundary and the upwelling stabilize at the center of the convection cell, and a trapped state emerges [Fig. 6(d)].

We find that the transition from an oscillatory state to a trapped state occurs at a critical value of the boundary size, $d_c=0.576D$. The third panel in Fig. 4 shows the dynamics of the floating boundary and upwelling at this critical condition. The floating boundary sustains a marginal oscillation, with a constant amplitude that is given by initial conditions. There is no waiting period at the end walls. The smooth trajectories

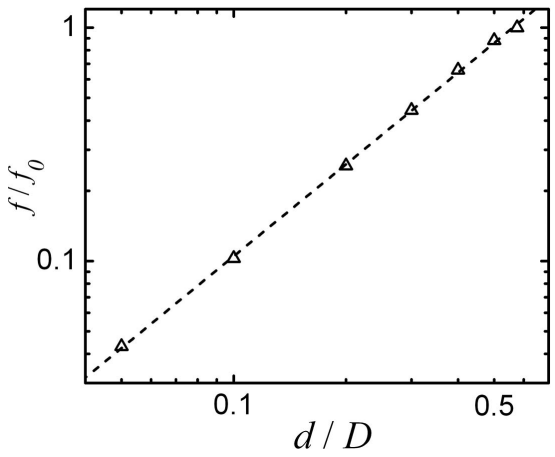

FIG. 7. Results from the model. In the oscillatory state, the normalized oscillation frequency is shown as a function of the coverage ratio. Over a finite range of floating boundary sizes, from 0.05D to d_c (0.576D), there appears to be a power-law dependence $f/f_0 \propto d^{1.31}$.

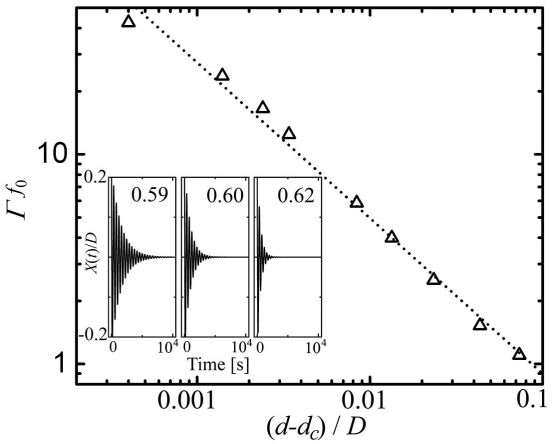

FIG. 8. In the trapped state, the normalized decay time Γf_0 is shown as a function of the coverage ratio. Inset: time series of the floating boundary motion in the trapped state. The data suggests a power law $\Gamma f_0 \propto (d-d_c)^{-0.768}$.

of both the floating boundary and the upwelling are quite close to harmonic oscillations.

Comparing with the experimental results (Fig. 3), our model seems to capture the most essential physical mechanisms and reproduces the oscillatory state and the trapped state. Moreover, the transition between the two states takes place at a similar value of $d/D \approx 0.6$. The intermittency observed in the experiment near the critical point (Fig. 3, $d/D=0.6$) and the small-amplitude stochastic motion in the trapped state (Fig. 3, $d/D=0.7$ and 0.8) are not recovered in the model.

In the oscillatory state, we compare the frequencies (defined to be $f=1/T$, T is the period of the oscillation) at different coverage ratios. As shown in Fig. 7, the normalized frequency follows the scaling $f/f_0 \propto d^{1.31}$, where f_0 is the frequency at the critical point. A previous full-scale Navier-Stokes numerical simulation of a floating boundary above a thermal convection cell also found a power-law dependence of frequency on the boundary size [31].

In the trapped state, from a given initial position (on one side of the convection cell) the floating boundary oscillates with decreasing amplitude. We find that the decay rate of the amplitude also depends on the boundary size. The dimensionless decay time Γ is defined as the time it takes for the original amplitude to reduce by a factor of e. Time Γ is infinite at the critical point, and decreases rapidly with increased coverage ratio, as shown in Fig. 8. The decay time follows the scaling law $\Gamma \propto (d-d_c)^{-0.768}$.

V. STABILITY ANALYSIS OF THE MODEL

The following discussion presents a detailed analysis of the dynamical system described by Eq. (7). We pay close attention to the stability of the floating boundary and the upwelling near the central region of the convection cell where both $X(t)$ and $Y(t)$ are small. Stable solutions from Eq. (7) correspond to the trapped state and unstable solutions correspond to the oscillatory state. The critical condition for the dynamical transition is obtained analytically.

A. Analysis of the finite difference scheme

In the finite difference scheme applied here, we let $X_n = X(n\Delta t)$. The dynamical equation (7) takes the form

$$\frac{X_{n+1}-X_n}{\Delta t} = \frac{1}{d+\gamma\lambda/w}[(2v_0+(D-d)\theta)(X_n-Y_n) - d\theta X_{n-\tau/\Delta t}],$$
$$\frac{Y_{n+1}-Y_n}{\Delta t} = d\beta(X_n-Y_n). \tag{9}$$

We set the time step, Δt, to be one second for convenience. Eliminating Y, one derives an iteration equation for X_n

$$X_n = C_1X_{n-1} + C_2X_{n-2} + C_3X_{n-\tau-1} + C_4X_{n-\tau-2} \tag{10}$$

with coefficients

$$C_1 = 2-\beta d + \frac{2v_0+\theta(D-d)}{d+\gamma\lambda/w},$$

$$C_2 = \beta d - 1 - \frac{2v_0+\theta(D-d)}{d+\gamma\lambda/w}, \quad C_3 = \frac{-d\theta}{d+\gamma\lambda/w},$$

and

$$C_4 = \frac{\theta(d\beta-1)d}{d+\gamma\lambda/w}$$

For the time before the floating boundary collides with the sidewalls, we can solve Eq. (10) explicitly

$$X_n = \sum_{i=1}^{\tau+2} a_i\lambda(d)_i^n. \tag{11}$$

Eigenvalues $\lambda(d)_i$ are roots of the characteristic equation

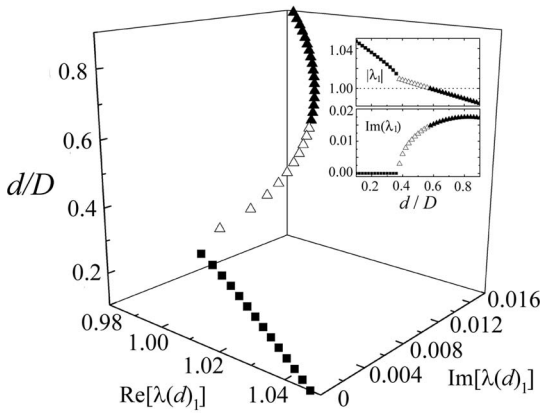

FIG. 9. A 3D plot of $\mathrm{Re}[\lambda(d)_1]$ and $\mathrm{Im}[\lambda(d)_1]$ as functions of the coverage ratio $(0.1<d/D<0.9)$. When $|\lambda(d)_1|<1$ (solid triangles), the system is in the trapped state. Open triangles indicate the oscillatory state where $|\lambda(d)_1|>1$ and $\mathrm{Im}[\lambda(d)_1]$ is nonzero. The system executes oscillations with increasing amplitude. As d/D is further increased, shown with solid squares, $|\lambda(d)_1|>1$ and $\mathrm{Im}[\lambda(d)_1]=0$. Here, the system first shows monotonic divergence and it is finally forced into periodic motion. The insets show $|\lambda(d)_1|$ and $\mathrm{Im}[\lambda(d)_1]$ as monotonic functions of the coverage ratio.

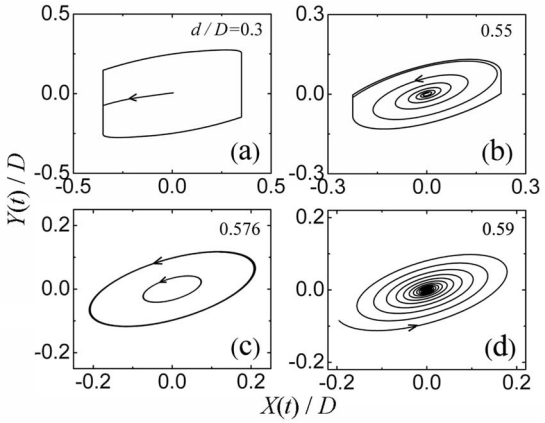

FIG. 10. Simulation data showing the trajectories of the moving boundary and the upwelling in the X-Y plane. The arrows show the directions of the evolution. Coverage ratios are chosen to be 0.3, 0.55, 0.576, and 0.59. They correspond to periodic orbits $(d/D=0.3$ and 0.55), a limit cycle $(d/D=0.576)$, and a stable focus $(d/D=0.59)$. At the critical size (c), two arbitrary initial amplitudes of the oscillation are retained in time.

(10). The constants a_i are determined by the initial values $X_m|_{m=0,1,\ldots,\tau+1}$. The solution for Y is

$$Y_n = b_0\sum_{i=1}^{\tau+2} a_i\lambda(d)_i^n + b_1\sum_{i=1}^{\tau+2} a_i\lambda(d)_i^{n-1} + b_2\sum_{i=1}^{\tau+2} a_i\lambda(d)_i^{n-\tau-1} \tag{12}$$

with the coefficients

$$b_0 = \frac{(d\beta-1)(d+\gamma\lambda/w)}{2v_0+\theta(D-d)}, \quad b_1 = 1-\frac{(d\beta-1)(d+\gamma\lambda/w)}{2v_0+\theta(D-d)}$$

and

$$b_2 = \frac{(\beta d-1)d\theta}{2v_0+\theta(D-d)}.$$

We arrange the eigenvalues $\lambda(d)_\iota$' s in order of decreasing absolute values

$$|\lambda(d)_i| \geqslant |\lambda(d)_j| \quad \text{if } i<j. \tag{13}$$

The local stability of the system depends on the absolute value of the eigenvalues. According to Eq. (13), the greatest eigenvalue, $|\lambda(d)_1|$, represents the dominate growth rate of X_n and Y_n. In Fig. 9, we plot $\lambda(d)_1$ as a function of the boundary size d.

For sufficiently large d, $|\lambda(d)_1|<1$, corresponding to a stable iteration where the system converges to the fixed point, which is the center of the convection cell. When the boundary size decreases, $|\lambda(d)_1|$ increases. Below the critical point, $d<d_c=0.576D$, $|\lambda(d)_1|$ becomes larger than 1. The imaginary part of $\lambda(d)_1$ is nonzero for $d>0.373D$. When d is in this range, the floating boundary starts to oscillate with increasing amplitude until it collides with the sidewall. As d further decreases, another bifurcation is found at $d/D=0.373$, below which the imaginary part of $\lambda(d)_1$ becomes zero while $|\lambda(d)_1|$ is still greater than one. Here, the solutions for X_n and Y_n diverge monotonically, and the floating boundary drifts directly toward one of the sidewalls.

We present in the X-Y plane the trajectories of both the floating boundary and the upwelling in Fig. 10. At sufficiently small coverage ratio $(d/D=0.3, |\lambda(d)_1|>1, \mathrm{Im}[\lambda(d)_1]=0)$, the floating boundary moves from the center to one sidewall, and then undergoes periodic oscillations [Fig. 10(a)]. As the coverage ratio increases, but while still below the critical value $(d/D=0.55, |\lambda(d)_1|>1, \mathrm{Im}[\lambda(d)_1]\neq 0)$, the center of the cell is still an unstable fixed point. The trajectory diverges gradually in spirals until it reaches the sidewalls, as shown in Fig. 10(b). After arriving at the sidewall, the trajectory is forced into a periodic orbit. Right at the transition point $[d=d_c=0.576D, |\lambda(d)_1|=1]$, the trajectory is a limit cycle whose oscillation amplitude stays constant at its arbitrary initial value [Fig. 10(c)]. When the coverage ratio further increases to be 0.59 $(|\lambda(d)_1|<1)$, the trajectory converges to the center and a trapped state appears [Fig. 10(d)].

B. Analytical solutions of the linear delay differential equation

Delay differential equations (DDE) have recently drawn much attention because many physical and biological systems involve feedback mechanisms with delays [39]. The above numerical results can be obtained from an analytical solution of the dynamical equation (7) treated as a linear DDE. The following analysis again shows that the system experiences a transition from a convergent state into a divergent state as the control parameters vary continuously.

It can be shown that Eq. (7) is equivalent to the following second order linear delay differential equation:

$$\ddot{X}(t) + (c-a)\dot{X} + bcX(t-\tau) + b\dot{X}(t-\tau) = 0, \quad t > 0,$$
$$X(t) = \varphi(t), \quad 0 \geqslant t \geqslant -\tau. \tag{14}$$

The initial conditions are given by $\varphi(t)$. The coefficients a, b, and c are functions of d

$$a = [2v_0 + \theta(D-d)]/(d + \gamma\lambda/w), \quad b = -d\theta/(d + \gamma\lambda/w), \tag{15}$$
$$c = d\beta.$$

When $t \to \infty$, the asymptotic behavior [40,41] of $X(t)$ is

$$X(t) = \sum_i p_i(t)e^{z_i t} + o(e^{z_i t}), \tag{16}$$

where $p_i(t)$ is a polynomial that depends on $\varphi(t)$ and z_i is the ith complex root of the following characteristic equation for Eq. (14):

$$f(z) = z^2 + (c-a)z + b(z+c)e^{-z\tau} = 0. \tag{17}$$

The roots $z_i(d,\tau)$ of $f(z)$ are continuous functions of the parameters d and τ. It has been proven that, as d or τ varies continuously, the number of roots of Eq. (17) that have positive real parts changes only after a pure imaginary root appears in the complex z plane [42–44]. So we can find a contour in the d-τ plane along which $f(z)$ has pure imaginary roots. This contour divides the d-τ plane into different regions. Within each region the number of roots with positive real parts remains constant.

When $\tau=0$ Eq. (17) becomes a quadratic equation and the solutions are

$$z_{1,2} = \frac{1}{2}[(a-b-c) \pm \sqrt{(c+b-a)^2 - 4bc}]. \tag{18}$$

At $d=0.553D$, $a(d)-b(d)-c(d)=0$, and $(c+b-a)^2-4bc<0$, there is a pair of conjugate roots on the imaginary axis on the complex plane. We thus find that on the d axis (when $\tau=0$) of the d-τ plane

$$\mathrm{Re}(z)_{\tau=0} \begin{cases} >0, & d < 0.553D, \\ <0, & d > 0.553D. \end{cases} \tag{19}$$

When $\tau>0$, the characteristic equation (17) is transcendental and has infinitely many roots in the complex z-plane. Let $z = \eta + i\xi$. Equation (17) becomes

$$\eta^2 - \xi^2 + (c-a)\eta + be^{-\eta\tau}[(\eta + c)\cos(\xi\tau) + \xi\sin(\xi\tau)] = 0, \tag{20}$$

$$2\eta\xi + (c-a)\xi + be^{-\eta\tau}[-(\eta + c)\sin(\xi\tau) + \xi\cos(\xi\tau)] = 0. \tag{21}$$

The values of d and τ for which the characteristic equation (17) has pure imaginary roots are given by the solutions of Eqs. (20) and (21) with $\eta=0$:

$$-\xi^2 + b[c\cos(\xi\tau) + \xi\sin(\xi\tau)] = 0, \tag{22}$$

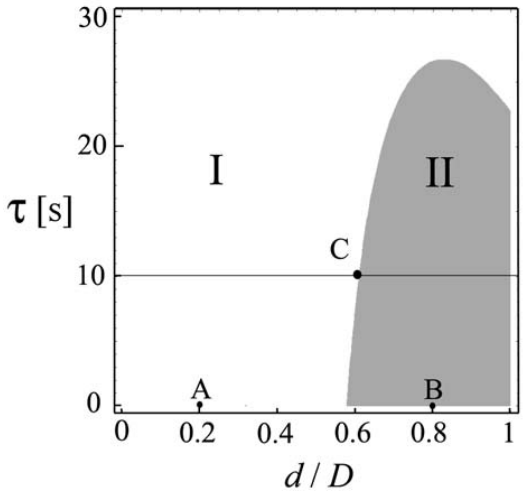

FIG. 11. Phase diagram for the stability of the system. The boundary between regions I (blank) and II (gray) is determined by the zero-contour of $F(d,\tau)$ from Eq. (25). We consider first the stability of the system with combinations of (d,τ) at points A ($d=0.2D, \tau=0$), and B ($d=0.8D, \tau=0$), from which we find that region I (II) corresponds to an oscillatory (trapped) state. The contour crosses the straight line ($\tau=10$ s) at C ($d=0.576D, \tau=10$ s), which determines the critical value of the transition. With sufficient large delay time, $\tau>26.5$ s, the system stays always in the oscillatory state (region I).

$$(c-a)\xi + b[\xi\cos(\xi\tau) - c\sin(\xi\tau)] = 0. \tag{23}$$

We solve for ξ explicitly from Eqs. (22) and (23), which depends only on d (note that a, b and c are functions of d).

$$\xi|_{\eta=0} = \pm\left\{\frac{1}{2}\sqrt{[(c-a)^2 - b^2] + 4b^2c^2} - \frac{1}{2}[(c-a)^2 - b^2]\right\}^{1/2} \tag{24}$$

We define a function $F(d,\tau)$ according to Eq. (22), where

$$F(d,\tau) = F(\xi(d),\tau) = -\xi^2 + b[c\cos(\xi\tau) + \xi\sin(\xi\tau)] \tag{25}$$

with ξ given by Eq. (24) [note that $F(\xi)$ is an even function of ξ]. Figure 11 shows that the zero contour of $F(d,\tau)$ divides the d-τ plane ($0 \leqslant d \leqslant D, 0 \leqslant \tau \leqslant 30$ s) into two regions. In region I, $F(d,\tau)>0$ and in region II $F(d,\tau)<0$.

Now we discuss the transition of the system when the control parameter d varies and when $\tau=10$ s. We study first the stability of the system with (d,τ) at two points, A and B at $\tau=0$. From Eq. (19), the system is unstable at A ($d=0.2D, \tau=0$) since $\mathrm{Re}[z(A)]>0$. While at B ($d=0.8D, \tau=0$), $\mathrm{Re}[z(B)]<0$ shows that the system is in a stable state.

As d and τ vary in the vicinity of B, the real parts of all the roots remain negative unless they cross the zero contour of $F(d,\tau)$. Roots at B ($d=0.8D, \tau=0$) can approach continuously the right part of the straight line $\tau=10$ s($d>d_c$). We conclude that for all roots, $\mathrm{Re}[z_i(d>0.576D, \tau=10\ \mathrm{s})]<0$. The asymptotic behavior of $X(t)$ in Eq. (16) is thus conver-

gent. Roots near A ($d=0.2D, \tau=0$) can approach the left part of the straight line $\tau=10$ s($d<d_c$), without crossing the zero contour of $F(d,\tau)$. So the number of the roots with positive real part remains the same as that of $f[z(\mathrm{A})]$. There are two roots with positive real parts when $d<0.576D$ and $\tau=10$ s, thus the system is in a divergent state. Finally the zero contour of $F(d,\tau)$ crosses the straight line $\tau=10$ s at C ($d=0.576D, \tau=10$ s), which shows the critical value for the transition in the system $d_c=0.576D$.

VI. DISCUSSION

Our present work models the interaction between a freely moving floating boundary and a convective fluid. Inside a Bénard convection cell, two counter-rotating convective circulations are induced and covered partially by a rigid boundary that is allowed to move freely on the fluid surface. Rich dynamics are found from the model and they are in excellent agreement with the previous experiments. The dynamical behaviors include regular oscillations of a small floating boundary, and the corresponding oscillations of the two large-scale circulations. When the floating boundary is large enough, a trapped state emerges; both the position of the floating boundary and the flow pattern in the bulk are stable.

In the model, we use a number of approximations that reflect the physical mechanisms involved in the coupled solid-fluid system. They are (1) the motion of the floating boundary is overdamped so that the speed is linearly proportional to the net force applied by the viscous flows; (2) the fluctuations of the large-scale circulations are averaged out so that no stochastic component is considered in the model; (3) the flow speed of each circulation depends linearly on its exposed fluid surface; and (4) due to thermal blanketing, the floating boundary constantly attracts the upwelling and the speed of the upwelling migration is proportional to the distance between them.

The above simplifications are justified by our previous experimental results. The model successfully explains the transition between the observed dynamical states; our simple model apparently captures the essential features of the coupling between the thermal blanket and the convecting fluid. We believe that this low-dimensional approach can bridge the gap between full-scale simulations and both laboratory experiments and geophysical observations.

Some aspects of the coupled dynamics observed in the experiment, such as the intermittency between the two states (Fig. 3), are not reproduced from our current model. This intermittent state is possibly due to the fluctuations in the velocity field of the fluid. In fact, one sees the effects of fluctuation from the turbulent flows by observing the stochastic motion of the floating boundary in the trapped states (Fig. 3, $d/D=0.7$ and 0.8). It has been shown that the stability of a dynamical system can be affected by the presence of random fluctuations of finite intensity [45,46]. Further research will attempt to discern if the intermittency is due to thermal noise or some other feedback mechanism.

In the geophysical context, the interaction between large continents and the convective mantle result in continental aggregations and dispersals [16,27,47]. An earlier simulation has reported the appearance of a temporary trapped state in which a large continent remains stationary directly over an upwelling, surrounded by two downwelling flows [20]. However, such a trapped state is transitory and the continent soon moves off from the central upwelling after the two nearby downwellings are pushed aside. If a trapped state has existed in the past and behaved the way we observe in our system, this state may not have lasted for long because supercontinents tend to breakup due to the divergent stress by the upwelling convection applied at the base. The stronger and constant heating from the upwelling in line with the finite tensile yield stress of the continent will further provoke the continental breakup. In this sense, a trapped state of a supercontinent is destined to be followed by a breakage event.

The observed states from our model system and from previous experiments may result partly from the spatial constrains imposed by the lateral boundary condition. In particular, both the floating boundary and the flow pattern are restricted within limited spaces. We currently conduct similar experiments in an annular geometry, where the moving boundary and the convective flow structure experience periodic, open boundary conditions. This new effort may let us better simulate the dynamic Earth and we expect richer behaviors.

ACKNOWLEDGMENTS

We thank M. Shelley, A. Libchaber, T. Bringley, and S. Spagnolie for fruitful discussions. This experiment and analysis is supported by the Department of Energy (Contract No. DE-FG0288ER25053) and by a New York University start-up grant.

APPENDIX A

Our numerical model uses the following constants v_0, θ, $\gamma\lambda/w$, β, and τ. They are estimated from our experimental results. All the spatial dimensions are normalized by the length of the convection cell D. For instance, when a floating boundary of size $d=0.6D$ is introduced, the length of the open fluid surface on both sides is on average $S_i=0.2D$.

1. Estimate the values of v_0 and θ

Terms v_0 and θ in Eq. (6) are estimated from the measured dependence of v_r on free surface extension S_r, which is shown in Fig. 2(b), where v_0 is the offset and θ is the slope. The dashed line in Fig. 2(b) shows

$$v_0 = 0.55 \text{ cm/s} = 0.015D \text{ s}^{-1}, \tag{A1}$$

$$\theta = \Delta v_r/\Delta S_r = 0.075 \text{ s}^{-1}. \tag{A2}$$

They are determined with an emphasis on data points around $S=0.20D$ (7.3 cm), the value of S when the size of the floating boundary is near the critical size for the transition between the two states.

2. Estimate the ratio $\gamma\lambda/w$

The motion of the floating boundary is caused by the viscous drag from the convective flows applied at the base, as

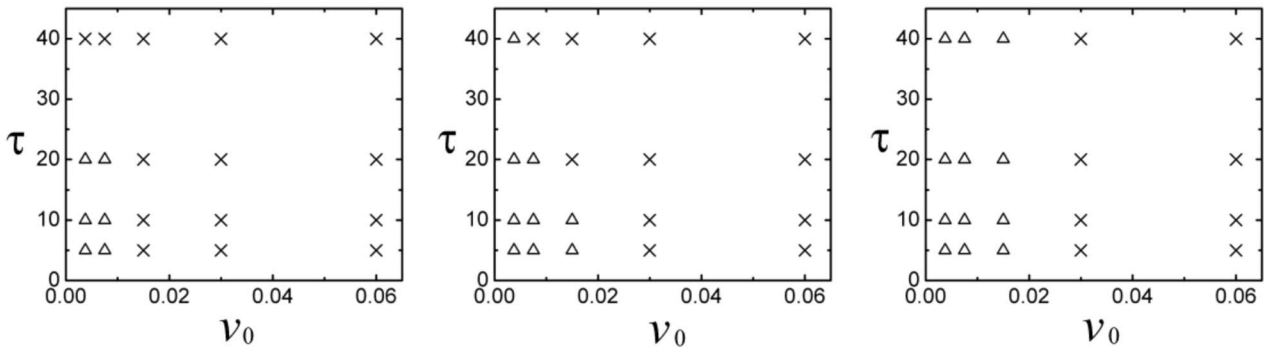

FIG. 12. Regime diagrams show the results from the model with different v_0 and τ, when $d/D=0.576$. The coefficient $\gamma\lambda/w$ in each panel from left to right is $1.44D$, $1.8D$, and $3.6D$. Crosses indicate values of v_0 and τ in which an oscillation state appears. Triangles indicate a trapped state.

shown in Eq. (1). Once in motion, the moving boundary experiences a viscous resistance from all edges. This resistance is proportional to its speed, as shown in the right-hand side of Eq. (3). Our experiment shows that the speed of the floating boundary saturates to a constant value after completing only 20% of the entire path towards the opposite end wall. This means that, during most of the time over the course of the boundary motion, the resistance and the viscous driving are in balance with each other. Thus Eq. (3) becomes the equation of motion.

We now estimate the ratio $\gamma\lambda/w$. In the oscillatory state near the critical point, $d=0.6D$, we measure experimentally [25] the maximum moving speed of the floating boundary $\dot{X}_{\max}$ and the mean flow speed of the circulation v_i, and find $\dot{X}_{\max}\approx 0.25v_i$. As the moving boundary proceeds and the upwelling is near its trailing edge, the boundary is subject to a single circulation underneath when a maximum speed is reached:

$$\dot{X}(t)=\frac{1}{d+\gamma\lambda/w}[v_r A_r(t)-v_l A_l(t)], \quad \dot{X}_{\max}\approx\frac{0.6Dwv_i}{0.6Dw+\gamma\lambda}.$$

We find

$$\frac{0.6D}{0.6D+\gamma\lambda/w}\approx\frac{\dot{X}_{\max}}{v_i}\approx 0.25, \quad \text{thus we have } \gamma\lambda/w\approx 1.8D. \tag{A3}$$

3. Estimate the proportional constant β

We observe that, in the oscillatory state and when the size of the floating boundary is close to $0.6D$, the time needed for the upwelling to migrate across the convection cell (during its half period of the oscillation) is

$$t_m\approx 100 \text{ s}.$$

From Eq. (5), $\dot{Y}(t)=d\beta[X(t)-Y(t)]$, we can estimate the value of β with

$$t_m\approx\frac{X-Y}{\dot{Y}}=\frac{1}{0.6D\beta} \quad \text{thus } \beta\approx\frac{1}{0.6Dt_m}\approx 0.017D^{-1}\ \text{s}^{-1}. \tag{A4}$$

4. Estimate the typical delay time τ

The response time τ of the circulation speed to a changed fluid surface is measured through a simple experiment. At $t=0$, the floater is relocated from one position ($S_r=5$ cm) to another ($S_r=10$ cm). This replacement itself takes up to 2 seconds. Before and after this action, the flow speed of the right-side circulation is recorded by a laser Doppler velocimetry. After averaging 30 trails of velocity time series, we get, as shown in Fig. 2(c)

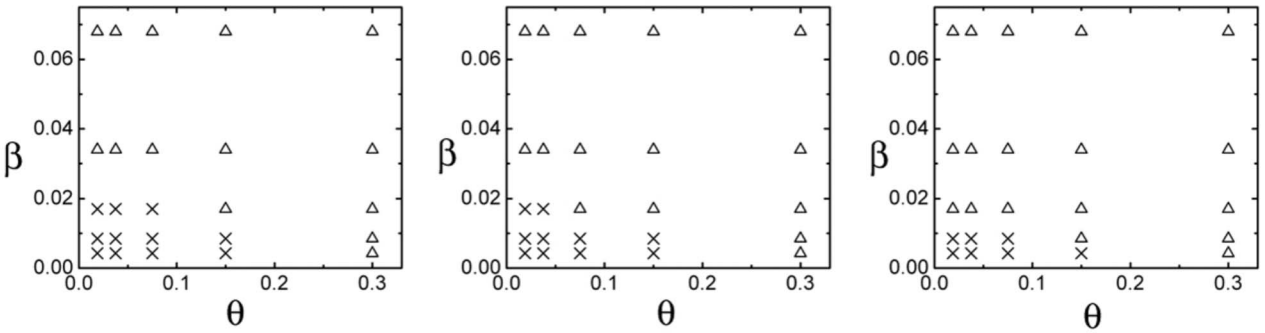

FIG. 13. Regime diagrams show the results from the model with different θ and different β. The coefficient $\gamma\lambda/w$ in each panel from left to right is $1.44D$, $1.8D$, and $3.6D$, when $d/D=0.576$. Crosses: oscillatory state. Triangles: trapped state.

$$\tau \approx 10 \text{ s}. \tag{A5}$$

To summarize, from the experiment we estimate the coefficients and constants needed in our model

$$(\gamma\lambda/w, v_0, \theta, \beta, \tau) = (1.8D,\ 0.015D\ \text{s}^{-1},\ 0.075\ \text{s}^{-1},\ 0.017D^{-1}\ \text{s}^{-1},\ 10\ \text{s}). \tag{A6}$$

APPENDIX B

Geophysical investigations show that changes in the thermal and mechanical properties of the continents are important factors in determining the evolution of the convective flow structures in the mantle, which, in turn, influence the continental motion [22,23]. We have worked on different models, systematically varying the boundary geometry factor γ, the flow response time τ, flow velocity offset v_0, the flow strength response rate θ, and the coefficient of the migration speed of the upwelling β from the values given in Eq. (A6). We study their influences on the dynamical states of the system.

We find that a higher offset of the mean flow speeds v_0 facilitates oscillatory motions. On the other hand, a thicker floating boundary (that is, a larger geometry factor γ) favors trapped states, since a larger resistant force is applied at the lateral edges of the floating boundary. Our calculations also show that a longer flow response time τ favors the oscillatory state, as indicated also in Fig. 11.

Figure 12 shows a regime diagram for the model with different boundary geometry factors γ, flow velocities v_0, and response times τ. Oscillatory states are shown by crosses, and trapped states are shown by triangles. In Fig. 12, the boundary geometry factor γ increases incrementally from the left panel to the right. Increasing γ produces a wider phase space for the trapped state.

It is known that the speed of the large-scale circulation in turbulent thermal convection with $\text{Pr} \approx 1$ depends on the Rayleigh number as $v_i \propto Ra^{4/9}$ [4]. As a test measurement in the experiment, near the critical point $d=0.6D$ we increase Ra by increasing the temperature difference ΔT by 5% (thus increasing Ra by 5%). We find the motion of the floating boundary changes from the intermittent state (Fig. 3, when $d/D=0.6$) to the oscillatory state (similar to that of Fig. 3, when $d/D=0.5$).

We also study the behavior of the coupled system on the θ-β diagram. A large contrast in the heat flux through the floating boundary and through the open fluid surface increases the rate of change of the flow strength θ, and also accelerates the migration speed of the upwelling β. Figure 13 indicates that a stronger thermal blanketing effect favors the trapped state.

[1] B. Castaing, G. Gunaratne, F. Heslot, L. Kadanoff, A. Libchaber, S. Thomae, X.-Z. Wu, S. Zaleski, and G. Zanetti, J. Fluid Mech. **204**, 1 (1989).

[2] M. C. Cross and P. C. Hohenberg, Rev. Mod. Phys. **65**, 851 (1993).

[3] E. D. Siggia, Annu. Rev. Fluid Mech. **26**, 137 (1994).

[4] S. Grossmann and D. Lohse, J. Fluid Mech. **407**, 27 (2000); Phys. Rev. Lett. **86**, 3316 (2001).

[5] The heat transport efficiency is expressed by the Nusselt number Nu. In thermal convection, the external thermal drive is characterized by the Rayleigh number Ra, Prandtl number Pr, and the aspect ratio of the convection cell. Recent work on the dependence of the Nusselt number on Ra and Pr can be found in Ref. [4], and references therein. References on the effects of the aspect ratio can be found in Refs. [6,7].

[6] Z. A. Daya and R. E. Ecke, Phys. Rev. Lett. **87**, 184501 (2001).

[7] S. Grossmann and D. Lohse, J. Fluid Mech. **486**, 105 (2003).

[8] Y.-B. Du and P. Tong, Phys. Rev. Lett. **81**, 987 (1998).

[9] K.-Q. Xia and S.-L. Lui, Phys. Rev. Lett. **79**, 5006 (1997).

[10] K.-Q. Xia and X.-L. Qiu, Europhys. Lett. **46**, 171 (1999).

[11] R. Verzicco, Phys. Fluids **16**, 1965 (2004).

[12] R. Krishnamurti and L. N. Howard, Proc. Natl. Acad. Sci. U.S.A. **78**, 4 (1981).

[13] T. H. Solomon and J. P. Gollub, Phys. Rev. A **43**, 6683 (1991).

[14] C. Sun, H.-D. Xi, and K.-Q. Xia, Phys. Rev. Lett. **95**, 074502 (2005).

[15] E. Brown, A. Nikolaenko, and G. Ahlers, Phys. Rev. Lett. **95**, 084503 (2005).

[16] D. L. Turcotte and G. Schubert, *Geodynamics* (Cambridge University Press, New York, 2002).

[17] J. Elder, Sci. Prog. **56**, 1 (1968).

[18] L. N. Howard, W. V. R. Malkus, and J. A. Whitehead, Geophys. Fluid Dyn. **1**, 123 (1970).

[19] J. A. Whitehead, Phys. Earth Planet. Inter. **5**, 199 (1972).

[20] M. Gurnis, Nature (London) **332**, 695 (1988).

[21] M. Gurnis and S. Zhong, Geophys. Res. Lett. **18**, 581 (1991).

[22] J. P. Lowman and G. T. Jarvis, Geophys. Res. Lett. **20**, 2087 (1993).

[23] J. P. Lowman and G. T. Jarvis, Phys. Earth Planet. Inter. **88**, 53 (1995).

[24] J. Zhang and A. Libchaber, Phys. Rev. Lett. **84**, 4361 (2000).

[25] J.-Q. Zhong and J. Zhang, Phys. Fluids **17**, 115105 (2005).

[26] J.-Q. Zhong and J. Zhang, Phys. Rev. E **75**, 055301(R) (2007).

[27] D. L. Anderson, Nature (London) **297**, 391 (1982).

[28] C. Grigné and S. Labrosse, Geophys. Res. Lett. **28**, 2707 (2001).

[29] The viscous drag on a thin plate perpendicular to a slow viscous flow is $8\pi C\eta U$, where U is the flow speed. Constant C happens to be the electrical capacity of a conductor in the same shape of the plate, which depends only on the dimensions of the plate. See, for example: R. Roscoe, Philos. Mag. **40**, 338 (1949).

[30] T. Yanagisawa and Y. Hamano, Proc. Jpn. Acad., Ser. B: Phys. Biol. Sci. **79**, 99 (2003).

[31] The time scale for the flow pattern evolution is shown to de-

pend on the size of the floating boundary. A systematic numerical investigation shows a power-law relationship between the flow reversal time and the boundary size: A. M. Bobrov, W. Jacoby, and V. P. Trubitsyn, J. Geophys. **27**, 133 (1999).
[32] X.-L. Qiu and P. Tong, Phys. Rev. E **64**, 036304 (2001).
[33] X.-L. Qiu, X.-D. Shang, P. Tong, and K.-Q. Xia, Phys. Fluids **16**, 412 (2004).
[34] J. B. Keller, J. Fluid Mech. **26**, 599 (1966).
[35] D. L. Turcotte and E. R. Oxburgh, J. Fluid Mech. **28**, 29 (1967).
[36] P. Welander, J. Fluid Mech. **29**, 17 (1967).
[37] L. Guillou and C. Jaupart, J. Geophys. Res. **98**, 12219 (1995).
[38] As shown in Fig. 2(a), the lengths of the floating boundary that lie on top of either circulation on both sides are $A_l(t)=d/2-X(t)+Y(t)$, $A_r(t)=d/2+X(t)-Y(t)$. The lengths of the open surfaces on either side of the floating boundary are $S_l(t)=(D-d)/2+X(t)$, $S_r(t)=(D-d)/2-X(t)$. Occasionally, when the floating boundary is small, the upwelling is outside of the boundary's edges ($|X-Y|>d/2$). In these cases we use different expressions for A_i and S_i. For example, when $X-Y>d/2$, $A_l=0$, $A_r=d$, $S_l(t)=Y(t)+D/2$ and $S_r(t)=D/2-d-Y(t)$.
[39] Recent research work on delayed differential equations can be found, for example, J. Belair and S. A. Campbell, SIAM J. Appl. Math. **54**, 1402 (1994); J.-J. Wei and S.-G. Ruan, Physica D **130**, 255 (1999); W. Yao, P. Yu, and C. Essex, Phys. Rev. E **63**, 021902 (2001).
[40] R. Bellman and K. L. Cooke, *Differential-Difference Equations* (Academic Press, New York, 1963).
[41] S. M. V. Lunel, *Exponential Type Calculus for Linear Delay Equations* (Centre for Mathematics and Computer Science, Amsterdam, 1989).
[42] J. Dieudonne, *Foundations of Modern Analysis* (Academic Press, New York, 1960).
[43] K. L. Cooke, J. Math. Anal. Appl. **86**, 592 (1982).
[44] X.-G. Li, S.-G. Ruan, and J.-J. Wei, J. Math. Anal. Appl. **236**, 254 (1999).
[45] R. N. Mantegna and B. Spagnolo, Phys. Rev. Lett. **76**, 563 (1996).
[46] M. Gitterman, *The Noisy Oscillator* (World Scientific, Singapore, 2005).
[47] J. T. Wilson, Nature (London) **211**, 676 (1966).